Hydrodynamic characterization of the aging induced performance degradation of HMX-based explosive PBX 9404

Scott I. Jackson
Department of Aerospace Engineering
Texas A & M University
College Station, TX USA

Carlos Chiquete and Eric K. Anderson
Shock and Detonation Physics Group
Los Alamos National Laboratory
Los Alamos, NM, USA

1 Introduction

Energetic materials are commonly able to store large amounts of potential energy for engineering applications. Energetics with complex molecular structures generally have the highest energy densities. In practice, they are deployed as explosive formulations consisting of combinations of several different compounds in a heterogenous matrix to achieve specific requirements (energy density, insensitivity to mechanical insult). Examples include Composition B, which consists of TNT, RDX and small amounts of wax, and PBX 9501, which consists of HMX, Estane, and BDNPA-F.

It is possible for these different compounds to chemically evolve during storage in a way that reduces their chemical potential energy. This can occur both from environmental degradation of individual compounds or from interactions between compounds in a given explosive formulation. The timescales of significant energy loss can be long (decades or more) making quantification of this effect challenging due to changes in diagnostic practices, equipment, test methods, and capability. However, accurate characterization of this energy loss is important for evaluation of the reliability of engineered explosive systems.

Formulations utilizing nitrocelluose are of particular concern due to the propensity of this material to decompose and release nitric acid, which further catalyzes the decomposition reaction and can also modify other compounds. A number of prior efforts [1, 2, 3, 4] have characterized the energy loss due to aging of the explosive PBX 9404, composed of 94 wt% HMX, 3 wt% tris-β chloroethylphosphate (CEF) plasticizer, 2.9 wt% nitrocellulose (NC), and 0.1 wt% diphenylamine (DPA) as a stabilizing agent [5].

Approximate energy methods quantified a distinct energy loss rate with age [4]. Hydrodynamic calculations provide the ability to relate this energy loss to the underlying thermodynamic properties of the detonation product equation of state (EOS), in particular the detonation product isentrope, which controls the energy delivery from the explosive products to confining materials. Preliminary attempts at this methodology confirmed the earlier results [4] through manual adjustment of the isentrope parameters [6].

Correspondence to: sij@tamu.edu

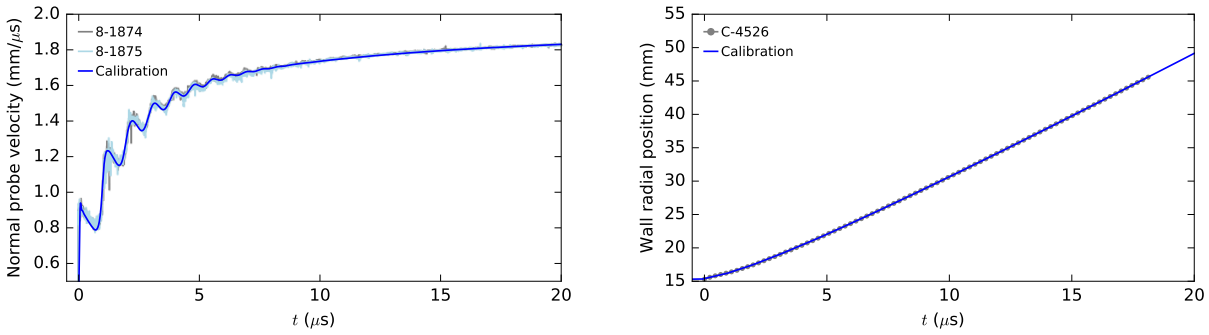

Figure 1: Left: The calibration calculation of the wall motion (for a normal PDV probe) and comparison to data for 8-1874 and 8-1875 [4]. Right: Streak wall expansion data and calibrated calculation for test C-4526 from [3]. The simulation resolution throughout was 125 microns.

Our present analysis builds upon this previous work using a programmed burn methodology that incorporates finite reaction zone effects and fully automated EOS calibration procedure for the most precise determination of the aging effect to date. The results infer how the detonation product isentrope changes with age.

2 Modeling analysis

PBX 9404 performance data including both streak and PDV diagnostics is available from [1, 2, 3, 4]. This data formed the basis of the previous analyses in [4, 6]. The more recent tests (within the last 15 years) used a PDV diagnostic and this data appears in Fig. 1 (left). One of these more modern tests (8-1293) included a streak diagnostic in addition to PDV. This "modern" streak data is compared to the much older streak data records (originally fielded in the 1970s) in Fig. 1 (right). Notably, the older streak data sampling rate is quite limited especially for the late time expansion. In general, the streak camera diagnostic is also known to lack the time resolution necessary to resolve the early time wall ringing evident in the PDV records [4].

To enable our new determination of the aging effect on PBX 9404's constitutive properties, a series of detonation performance model calibrations were conducted for each of the source data sets. We take advantage of modern programmed burn methodologies to calculate the detonation timing and energy delivery to the confiner. For timing, the Detonation Shock Dynamics (DSD) [7] model was used to generate a measure of the curvature effect on detonation propagation for this explosive. Typically, detonation timing component is calibrated to phase velocities and front shape measurements derived from bare axisymmetric cylindrical geometry (or "rate stick") tests. For PBX 9404, we use a series of unconfined rate stick tests reported in [5] and shown in Fig. 2. In contrast to the CYLEX tests, however, there is no equivalent multi-decade experimental series to diagnose any aging modification of this diameter-effect trend. Furthermore, detonation velocity trend with age from the CYLEX data (Fig. 2 left) may vary weakly with age but requires further analysis. Thus, the diameter effect trend and the limiting Chapman-Jouguet (CJ) detonation velocity are assumed constant in the present study.

The details of our DSD propagation law calibration methodology and numerical choices have been described and validated in [8] for the closely related HMX-based PBX 9501. The parameterized functional relation between the normal detonation velocity (D_n) and local surface curvature (κ) that we use is, $D_n(\kappa) = D_{CJ}(1 - B\kappa(1 + C_2\kappa + C_3\kappa^2)/(1 + C_4\kappa + C_5\kappa^2)$ where the $D_n - \kappa$ parameters (D_{CJ}, B, C_i for $i = 1, \ldots 5$) and the unconfined or sonic edge angle paramete (which sets the DSD

Table 1: The calibrated $D_n - \kappa$ parameters.

D_{CJ} (mm/μs)	B (mm)	C_2 (mm)	C_3 (mm^2)	C_4 (mm)	C_5 (mm^2)	ϕ_s (deg.)
8.790	0.06257	0.00027	0.04587	0.01205	0.00006	30

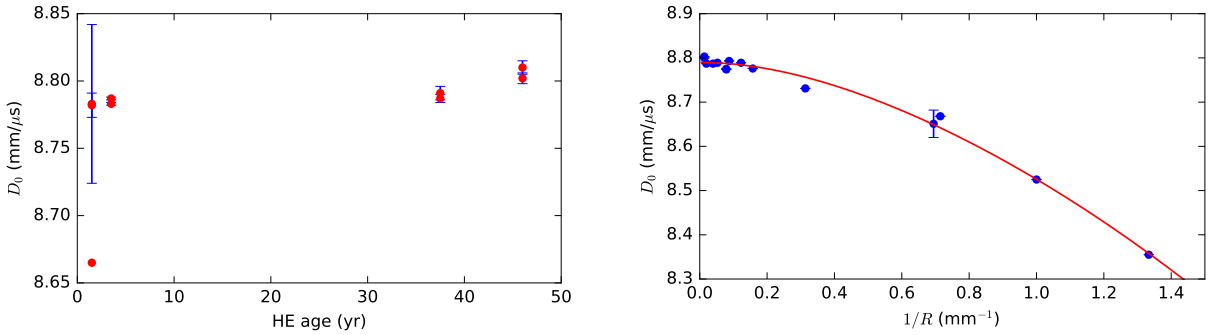

Figure 2: Left: The cylinder test phase velocity measurements and associated error bars plotted as function of HE age. Right: The diameter effect DSD calculation compared to the available phase velocity data.

calculation boundary condition) are given in Table 1. The limiting velocity parameter D_{CJ} was fixed in the calibration as informed by both the measured CYLEX velocities and the diameter effect data. Figure 2 (right) compares the computed diameter effect curve and the phase velocity measurements with excellent agreement.

In addition to timing, programmed burn methods require an energy release and products EOS model to determine the high explosive (HE) work done in a given hydrodynamic calculation. We use the VAJWL energy release method which is a modification of the Jones-Wilkins-Lee (JWL) equation of state (EOS) [9], augmented with energy deposition offsets that depend on the local, spatially-dependent DSD front detonation velocity (D_n) and time of arrival (t_b) to achieve a measure of the finite-reaction zone effect. The energy release model modifies the pressure (p) dependency on the local specific energy (e) and volume (v),

$$p(v,e) = (A + a(D_n))\left(1 - \frac{\omega v_0}{(R_1 + r_1(D_n))v}\right) \times \exp\left(-\frac{(R_1 + r_1(D_n))v}{v_0}\right) + B\left(1 - \frac{\omega v_0}{R_2 v}\right) \times \exp\left(-\frac{R_2 v}{v_0}\right) + \frac{\omega}{v}(e - e' - \lambda(t_b)E_{det}),$$

where A, B, R_1, R_2, E_{det} and ω are the base EOS model parameters, e' is a constant of integration such that $p(v_0, 0) = 0$ (standard convention in condensed-phase detonation where the ambient pressure is negligible relative to the post-shock values). Previously, we have developed an iterative multimaterial hydrodynamic code (or "hydrocode") process to refine the energy release and products EOS parameters of this model [10, 11, 12]. The DSD calculation for the CYLEX tests uses a value of 12 degrees to represent the confinement effect from the copper material (modeled via [13]).

The error metric for optimization is based on the RMS error of the comparison between data and calculation (for both the normal PDV probe velocity and streak). The non-normal probe wall velocity data sets from [2] tests were analytically corrected to a normal probe direction according to [14, 15, 16]. Parameters A, B, R_1, R_2 were optimized while ω was kept fixed and E_{det} was set to enforce $D_{CJ} = 8.79$ mm/μs for consistency with the $D_n - \kappa$ law-based propagation at each iteration. The found products

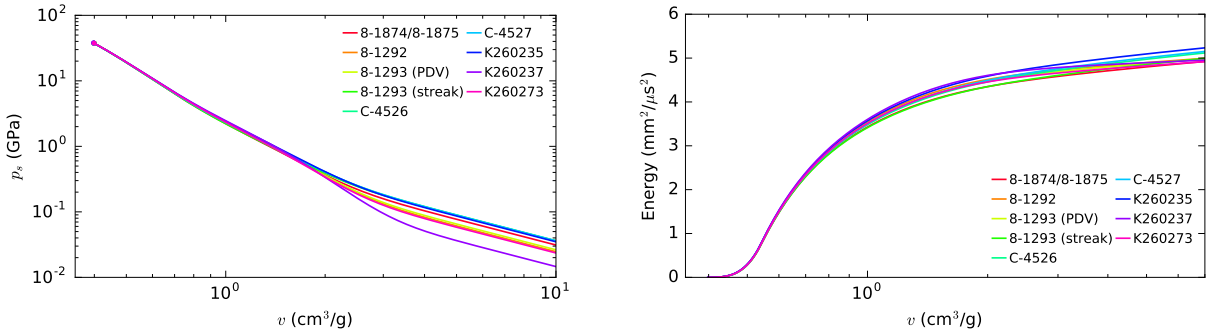

Figure 3: Left: The model pressure isentropes derived from the various data sets. The filled circle represents the CJ point. Right: Integrated energy delivery metric for the various models.

EOS model parameters and representative fit error values are tabulated in Table 2. Figure 1 (left) shows an example of the fit quality for the PDV-based calibration process (for 8-1874 and 8-1875) which results in a RMS error of 22.3 m/s. This error level is commensurate with the inherent probe variability in each signal. Figure 1 (right) does the same for a streak-based calibration (C-4526), finding an RMS error of about 19 microns. Shots K260235 and K260237 from the McMurphy data set produced larger fit errors ($2\times$) and the derived models are therefore somewhat less precise as a result.

Table 2: The calibrated EOS parameters for the various data sets. The parameter ω is considered fixed in the calibration and given the value of 0.3043 derived from [17]. Note that the Jackson tests (8-1874 & 8-1875) [4] were calibrated at once since the initial densities and experimental geometries were equivalent.

Shot ID	Diagnostic	RMS error	A (GPa)	B (GPa)	C (GPa)	R_1	R_2	E_{det} (kJ/g)	ρ_0 (g/cm^3)	p_{CJ} (GPa)	v_{CJ} (cm^3/g)
8-1874 8-1875	PDV	22.3 m/s	812.527	18.012	1.397	4.525	1.384	6.064	1.846	37.28	0.4001
8-1292	PDV	33.7 m/s	803.410	18.705	1.104	4.521	1.304	5.898	1.845	37.63	0.3989
8-1293	PDV	26.5 m/s	805.066	18.475	1.180	4.521	1.321	5.943	1.845	37.54	0.3993
8-1293	streak	35.1 μm	808.265	17.431	1.604	4.518	1.409	6.306	1.845	37.24	0.4004
C-4526	streak	18.9 μm	807.176	17.757	1.627	4.527	1.383	6.446	1.847	37.44	0.3994
C-4527	streak	23.3 μm	805.853	17.828	1.618	4.528	1.371	6.472	1.847	37.50	0.3991
K260235	streak	87.5 μm	783.570	18.184	1.565	4.500	1.350	6.513	1.845	37.82	0.3982
K260237	streak	68.0 μm	782.184	17.540	0.654	4.461	1.188	5.488	1.845	37.93	0.3978
K260273	streak	30.9 μm	806.512	18.892	1.054	4.525	1.317	5.782	1.843	37.50	0.3997

Figure 3 (left) shows how the many pressure isentropes produced in the calibration process tend to diverge (in relative terms) at larger volumes. The corresponding chemical energy or equivalently, the CJ isentrope energy (area under pressure isentrope curve but offset by the Rayleigh line energy), is plotted for all the models in Fig. 3 (right). As in the previous analyses in [4] and [6], the nominally repeat McMurphy tests generate a similar variability in energy delivery to the rest of the shots [2, 3, 4]. Similarly to [4, 6], Fig. 4 (right) shows the energy delivery values at a set expansion volume (7.0 cm^3/g) but plotted as function of HE age. A linear trend line is added to quantify the aging effect and its intercept is used to scale the energy and reveal the percent performance decrement over time. The negative slope of this line indicates a performance decrement over time, (e.g. $0.54 \pm 0.36\%$ energy loss/decade for $v = 7.0$ cm^3/g). However, the large relative standard error of the slope fit parameter also reflects a substantial uncertainty in this conclusion (up to 67% of the unperturbed value). However, Fig. 4 (left) also makes clear that much of the uncertainty is driven by the McMurphy data model reductions. If these are removed from consideration, the corresponding slope increases and the trend uncertainty

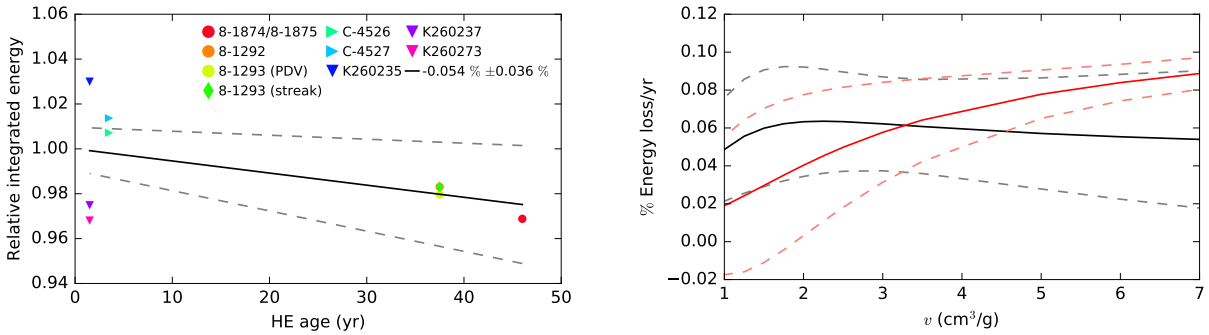

Figure 4: Left: The integrated energy metric evaluated at $v = 7.0$ cm^3/g and plotted as function of HE age. The dashed lines bound the trend line behavior due to uncertainty in the fit parameters. Right: The dependence of the aging effect on v when all data is considered (black) and when the McMurphy data sets are excluded (red).

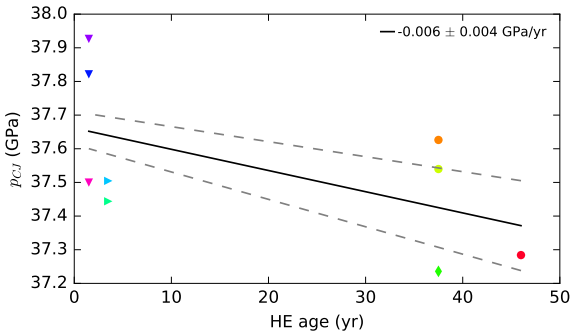

Figure 5: Right: The evolution of the CJ pressure for each model with HE age.

is greatly reduced, i.e. $0.89 \pm 0.08\%$ energy loss/decade. This same fitted slope (representing the strength of the aging effect) is plotted as function of v in Fig. 4 (right). This again shows how the large amount of scatter in the McMurphy data sets can affect these results. Without these data sets included in the analysis, the aging effect actually increases for larger expansion volumes as in [4]. For small volumes, the aging effect magnitude is minimized and the uncertainty in this parameter is increased. Using all the data however, the aging effect is much less variable and actually has a local maximum and small decreasing trend for most of the shown range in v (in similarity to [6]) but is near constant with expansion level. Finally, in Fig. 5 (right), a similar performance decrement trend is extracted from the CJ pressure variation with HE age but here the variability is more widespread than in the integrated energy measure.

This work builds on previous efforts to analyze this data in the context of HE aging via the use of modern detonation performance modeling methodologies and higher fidelity calibration processes. Consistent with this prior analysis, linear regression of the modeled energy delivery at relevant fixed specific volumes shows a measurable energy decrement and decrement in the CJ pressure with explosive age. While there is uncertainty in the magnitude of the energy loss rate due primarily due to the sparse dataset, this analysis does support degradation of both the explosive energy content and detonation CJ pressure with age.

References

[1] F. McMurphy. Cylinder tests of HE materials. Technical report, Lawrence Livermore National Laboratory, Livermore, CA USA, 1988.

[2] L. G. Hill, R. Mier, and M. E. Briggs. PBX 9404 detonation copper cylinder tests: A comparison of new and aged material. In *AIP Conference Proceedings*, volume 1195, pages 129–132. American Institute of Physics, 2009.

[3] A. Campbell and R. Engelke. Cylinder test comparison of PBX 9404, 9501, and x-0282. Technical report, Los Alamos National Laboratory, Los Alamos, NM USA, 1975.

[4] S. I. Jackson, E. K. Anderson, and L. G. Hill. Direct measurement of energy loss due to aging effects in the condensed phase explosive PBX 9404. *Proc. Combust. Inst.*, 37(3):3645–3652, 2019.

[5] T. R. Gibbs and A. Popolato. *LASL Explosive Property Data*. University of California Press, 1980.

[6] H. O. Wooten and V. H. Whitley. Analysis of historical and recent PBX 9404 cylinder tests using FLAG. Technical Report LA-UR-16-24389, Los Alamos National Laboratory, 2016.

[7] J. B. Bdzil, W. Fickett, and D. S. Stewart. Detonation shock dynamics: a new approach to modeling multi-dimensional detonation waves. In *Proc. 9th Intl. Symp. on Detonation*, pages 730–42, 1989.

[8] C. Chiquete, M. Short, E. K. Anderson, and S. I. Jackson. Detonation shock dynamics modeling and calibration of the HMX-based conventional high explosive PBX 9501 with application to the two-dimensional circular arc geometry. *Combust. Flame*, 222:213–232, 2020.

[9] E. Lee, M. Finger, and W. Collins. JWL equation of state coefficients for high explosives. Technical Report UCID-16189, Lawrence Livermore National Laboratory, 1973.

[10] C. Chiquete and S. I. Jackson. Detonation performance of the CL-20-based explosive LX-19. *Proc. Combust. Instit.*, 38(3):3661–3669, 2020.

[11] C. Chiquete, S. I. Jackson, E. K. Anderson, and M. Short. Detonation performance experiments and modeling for the DAAF-based high explosive PBX 9701. *Combust. Flame*, 223:382–397, 2020.

[12] E. K. Anderson, C. Chiquete, S. I. Jackson, R. I. Chicas, and M. Short. The comparative effect of HMX content on the detonation performance characterization of PBX 9012 and PBX 9501 high explosives. *Combust. Flame*, 230:111415, 2021.

[13] D. L. Preston, D. L. Tonks, and D. C. Wallace. Model of plastic deformation for extreme loading conditions. *J. Appl. Phys.*, 93(1):211–220, 2003.

[14] S. I. Jackson. The detonation cylinder test: Determination of full wall velocity and shape from a single velocimetry probe with an arbitrary angle. In *AIP Conference Proceedings*, volume 1793, page 050017. AIP Publishing LLC, 2017.

[15] S. I. Jackson. An analytic method for two-dimensional wall motion and product isentrope from the detonation cylinder test. *Proc. Combust. Inst.*, 35(2):1997–2004, 2015.

[16] S. I. Jackson. The dependence of ammonium-nitrate fuel-oil (ANFO) detonation on confinement. *Proc. Combust. Inst.*, 36(2):2791–2798, 2017.

[17] S. I. Jackson. Scaling of the detonation product state with reactant kinetic energy. *Combust. Flame*, 190:240–251, 2018.